

Atomic properties of sodium silicate glasses obtained from the building-block methodK. N. Subedi,^{1,*} V. Botu,^{2,†} and D. A. Drabold^{1,‡}¹*Department of Physics and Astronomy, Nanoscale and Quantum Phenomena Institute (NQPI), Ohio University, Athens, Ohio 45701, USA*²*Science and Technology, Corning Research and Development Corporation, Corning, New York 14830, USA*

(Received 16 September 2020; accepted 25 March 2021; published 8 April 2021)

Atomistic simulations of $(\text{Na}_2\text{O})_x(\text{SiO}_2)_{1-x}$ glasses are carried out using the building-block method that uses copies of low-energy units, “building blocks,” to build large realistic structural models. The calculated pair-correlation functions show that the local structure of these glasses is in good agreement with diffraction experiments. The electronic density of states for the doped models reveals defects in the band gap close to the conduction tail that are localized around undercoordinated Na atoms. Thermal properties for the systems, including the thermal expansion coefficient, are studied within the quasiharmonic approximation, and compare favorably with experiment. The elastic properties of the glasses are studied by calculating bulk and shear modulus.

DOI: [10.1103/PhysRevB.103.134202](https://doi.org/10.1103/PhysRevB.103.134202)**I. INTRODUCTION**

Sodium silicates $[(\text{Na}_2\text{O})_x(\text{SiO}_2)_{1-x}]$ are widely studied glasses that have established and potential applications for photonics, and biomaterial engineering [1–3]. Despite these applications, the atomic structure of these glasses is still not well understood, owing to the large number of possible local bonding environments because of the complex composition. To fully exploit these glasses for practical applications, fundamental insight about the atomic structure is needed. Experimental work such as extended x-ray absorption fine structure (EXAFS) spectroscopy [4], magic angle spinning NMR (MAS-NMR) [5,6], x-ray photoelectron spectroscopy (XPS) [7], and neutron diffraction [8] have determined many fingerprints of the structure. However, the fingerprints alone are insufficient to determine the microstructure. Computer simulations have become the preferred route to understanding such materials at the nanoscale. Most classical molecular dynamics (MD) and *ab initio* molecular dynamics (AIMD) studies have used the quench-from-melt scheme [9] to obtain the $(\text{Na}_2\text{O})_x(\text{SiO}_2)_{1-x}$ structures. Within this method, properties of densified silicates and the impact of the cooling rates on the structure of the silicates glasses have been discussed [10,11]. With *a priori* experimental information available, methods like force enhancement atomic refinement (FEAR) [12] can be used, which integrates experimental constraints with classical MD or AIMD to obtain more realistic models. A recent work by Zhou *et al.* [13] has employed the method to study $(\text{Na}_2\text{O})_{0.3}(\text{SiO}_2)_{0.7}$ glasses using classical MD. The study shows that FEAR models capture the medium-range order particularly well. Most of the earlier and contemporary works on $(\text{Na}_2\text{O})_x(\text{SiO}_2)_{1-x}$ [14–17] are primarily focused

on the structural character of the materials, and have been successful when compared to experiments. Limited literature is available on electronic, optical, and mechanical properties [18,19]. One interesting recent study of diffusion of the sodium silicate melt has been offered by Hung *et al.* [20], revealing that two different diffusion mechanisms could occur in such glasses. However, to our knowledge, there are no studies on the thermal properties, especially the thermal expansion coefficient (TEC), a key quantity for applications.

All amorphous materials have significant short-range order, some form of medium-range order, and ultimately no long-range order. Thus, amorphous silicon has local order very reminiscent of diamond: bond angles that are clustered around the tetrahedral angle and the great preponderance of bond lengths near the diamond nearest-neighbor distance. Similarly, glassy phases of SiO_2 consist of interconnected Si-O tetrahedra that nevertheless have bond-angle disorder in both Si-O-Si and O-Si-O angles (the latter again distributed around the tetrahedral angle). Other examples come to mind, such as the pyramidal units of As_2Se_3 . As the stoichiometry of the glass becomes complex when including several elements, the building blocks are not necessarily so simple. It is with this background that we are motivated to use the “building-block” method [21]. Essentially, we try to identify the complex units, and perform a melt-quench simulation with that local order already built in. To enable this, a small cell (here, 30 atoms) of the correct stoichiometry of the glass and low energy is obtained by a thorough and extensive annealing-quenching process (easy to carry out because the cell is so small). The idea is that the actual glass is likely to exhibit such local order. The small cell is then used to build a larger cell from eight copies of the small cell formed into a cube with 240 atoms. A melt-quench method is then carried out with this larger cell and remnants of this local order will persist even after a melt-quench process. This scheme has worked quite well in multinary glasses with complex ordering, and in particular seems to match or sometimes outperform the

*ks173214@ohio.edu

†botuv@corning.com

‡drabold@ohio.edu

conventional melt-quench method starting from random initial conditions, even for fairly extended simulations. The pair-correlation functions for the ternary glasses $\text{AsGe}_{0.8}\text{Se}_{0.8}$ and $\text{Ge}_2\text{As}_4\text{Se}_4$ have shown pleasing agreement with experiment [21]. A conceptually related but different version of the idea was presented by Ouyang and Ching, applied to amorphous Si_3N_4 glasses [22].

The rest of the paper is organized as follows. The computational methodology for obtaining the models and the quasiharmonic approximation are discussed in Sec. II. The structural, electronic, thermal, and elastic properties are described in Sec. III.

II. METHODOLOGY AND COMPUTATIONAL DETAILS

A. Generation of models using building-block method

AIMD simulations were performed using the Vienna *Ab initio* Simulation Package (VASP) [23]. Three atomic models of $(\text{Na}_2\text{O})_x(\text{SiO}_2)_{1-x}$ were made with $x = 0.0, 0.1, \text{ and } 0.3$. For each model, a small “subunit cell” was built with 30 atoms at the known experimental density [24] and desired stoichiometry. The atoms were randomly placed with minimum separation of 2.1 \AA from each other. The temperature of the subunit cell was then increased to 3500 K in 4.5 ps and equilibrated at this temperature for 6 ps . The “hot liquid” was then cooled in successive steps followed by equilibration for a few picoseconds to make the model representative of that temperature. Then it was cooled to 2000 K at a cooling rate of $2 \times 10^{14} \text{ K/s}$ followed by equilibration for 7.5 ps at the same temperature. The equilibrated subunit cell was further cooled to 1000 K at the same cooling rate followed by another equilibration for 7.5 ps . The subunit cell was then quenched to 300 K and equilibrated for another 7.5 ps . The conjugate gradient (CG) method as implemented in VASP was then used to relax the subunit cell to optimize its energy. At least four such relaxed subunit cells were obtained by repeating the process and the subunit cell corresponding to the lowest energy termed as building block (BB) was considered for the further calculations. Eight copies of the BB were used to prepare the starting configuration of the supercell that consists of 240 atoms. Following a similar scheme as used for the subunit cell, the supercell was annealed at 2500 K for 7.5 ps and quenched to 300 K .¹ The model was then equilibrated at 300 K for 7.5 ps . The equilibrated model at 300 K was finally optimized by performing zero-pressure relaxation. This resulted in a nonorthogonal cell and thus the density of the supercell changes slightly (a variation in density was less than 3% for all models). A direct melt-quench model with $x = 0.3$ consisting of 240 atoms was also obtained for comparison. The initial structure was annealed from 300 to 3500 K in 4.0 ps and was equilibrated at 3500 K for 6 ps . It was then cooled to 2000 K at the same cooling rate of $2 \times 10^{14} \text{ K/s}$ followed by equilibration for 6 ps at 2000 K . The model was further cooled to 1000 K at the same cooling rate and was equilibrated for the next 4 ps . It was then quenched to 300 K

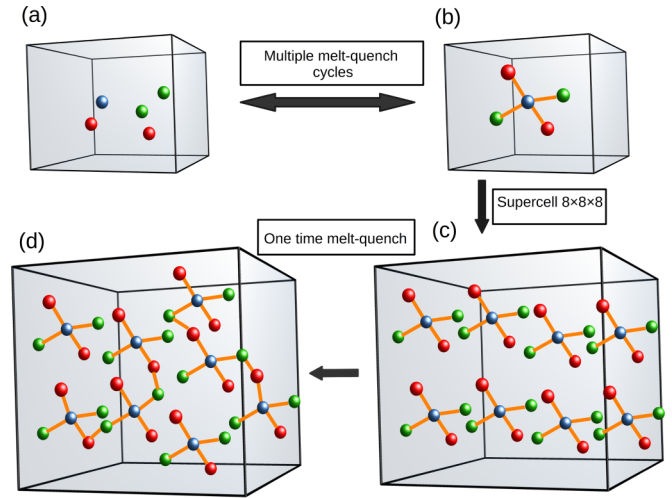


FIG. 1. Schematic flow chart for the building-block method. (a) Initial configurations of atoms in the subunit cell. (b) The subunit cell with minimum energy from several melt-quench cycles. (c) $8 \times 8 \times 8$ supercell formed from the optimized subunit cell. (d) The final model formed after one melt-quench cycle followed by relaxation.

followed by another equilibration for 4 ps . The model was finally optimized by performing zero-pressure relaxation. The direct melt-quench model was generated in $\approx 40 \text{ ps}$ in terms of simulation time scale. The BB model took $\approx 65\%$ of the time taken to generate the direct melt-quench model starting from the supercell of 240 atoms. This excludes the simulation time to prepare the optimized BB of a 30-atom cell that is very cheap for computation. In all the above calculations, plane-wave basis sets were used with a kinetic energy cutoff of 400 eV . For the CG and the zero-pressure relaxation steps, a cutoff of 520 eV was used. The generalized gradient approximation (GGA) of Perdew-Burke-Ernzerhof (PBE) [25] was used as the exchange-correlation functional. A single k point (Γ) was used to sample the Brillouin zone. In all MD calculations, a time step of 1.5 fs was used and the temperature was controlled by a Nosé-Hoover thermostat [26–28]. Gaussian smearing with a width of 0.05 eV was used to represent the partial occupancies of the energy levels near the Fermi level. Periodic boundary conditions were used throughout the calculations. The flow chart for the above discussed method is depicted in Fig. 1.

B. Quasiharmonic approximation

The thermal properties of the materials can be calculated within the framework of the quasiharmonic approximation (QHA). In this approach, the volume dependence is used to compute the approximate free energy $F(V, T)$, expressed as

$$F(V, T) = E_0(V) + F_{\text{vib}}(T, V), \quad (1)$$

where E_0 is the ground-state energy for a given volume V . E_0 is the density functional total energy (the potential energy of the configuration). F_{vib} represents the vibrational contribution to the free energy. Once the phonon frequencies over the

¹The α - SiO_2 model was annealed at 3000 K due to its higher melting point compared to silicate models.

Brillouin zone are known, F_{vib} is given by

$$F_{\text{vib}} = \sum_{qj} \hbar \omega_{qj} \left[\frac{1}{2} + \frac{1}{\exp(\hbar \omega_{qj}/k_B T) - 1} \right], \quad (2)$$

where ω_{qj} is the phonon frequency for a given wave vector q and the band index j ; T , k_B , and \hbar are the temperature, Boltzmann constant, and Planck's constant.

To implement this, the relaxed supercell vectors were gradually scaled by factors from 0.97 to 1.03 with a step of 0.01 to obtain seven different configurations for both doped models. Structural optimization was then performed for each model at fixed volume with the convergence criteria of 10^{-6} eV and 0.004 eV/Å for energy and force on each atom, respectively. Static calculations were performed for each configuration to obtain $E_0(V)$ for both models. To obtain the phonon frequencies, the displacement of atomic coordinates by 0.015 Å was made along the $\pm x$, $\pm y$, and $\pm z$ directions for each configuration. This led to several supercells being slightly distorted from equilibrium geometry. Every such displacement configuration was then treated by a single-point computation and the force calculation was performed in VASP. The forces were collected from each displacement and the phonon frequencies were calculated on $31 \times 31 \times 31$ mesh grids. The contribution of the phonon frequencies was then included to obtain $F(V, T)$. The Helmholtz free energy was fitted with the Birch-Murnaghan equation of state (EOS) [29,30]. Additional calculations were performed using PHONOPY [31], a convenient open-source package for phonon-related computations.

III. RESULTS AND DISCUSSION

A. Structural properties

The structural topology of $(\text{Na}_2\text{O})_x(\text{SiO}_2)_{1-x}$ models were analyzed by calculating pair-correlation functions, structure factors, bond angle distribution functions, Q^n distributions, and the coordination environment of each atomic species. The obtained results are compared with experiment and also with other available AIMD and classical MD results.

The left plot in Fig. 2 displays the total distribution function, $T(r)$, calculated from the models and obtained from the experiments for the undoped ($x = 0.0$) and the “fully” doped case ($x = 0.3$). The experimental data for the undoped and the doped models were taken from Refs. [32,33], respectively. $T(r)$ for the doped model with $x = 0.3$ shows excellent agreement up to the local-range order (≈ 3.4 Å) and is in pleasing agreement up to the medium-range order (5–6 Å). $T(r)$ for the doped model ($x = 0.3$) obtained from the direct melt-quench method is also displayed for comparison, and shows almost the same local ordering as the model obtained from the building-block method. $T(r)$ for the undoped model shows very good agreement with the experiment up to 3 Å and also accurately reproduces peaks in the medium-range order. The structure factor, $S(q)$, for both models ($x = 0.0$ and 0.3) was also calculated from the Fourier transform of the radial distribution function, $g(r)$, and is shown in the right-hand plot of Fig. 2. $S(q)$ for both models shows excellent agreement with the available experiments [33,34] other than first sharp diffraction peaks (FSDPs). $S(q)$ for the direct melt-quench model and using the reactive force-field (ReaxFF) potential

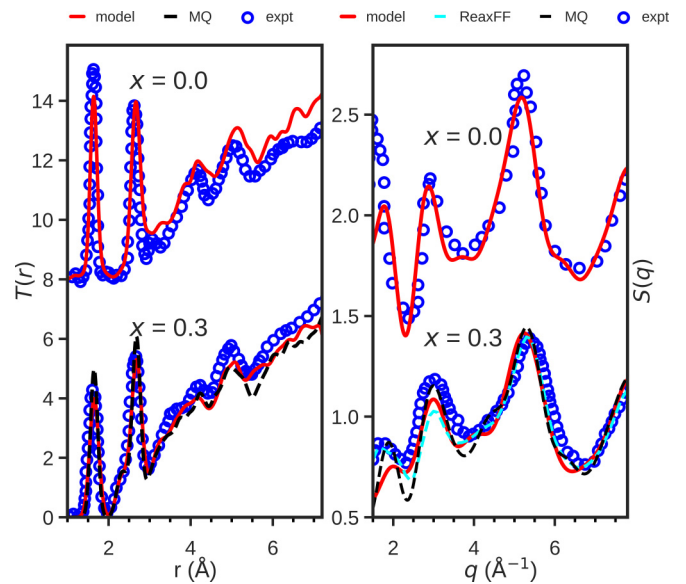


FIG. 2. Total distribution function $T(r)$ and the structure factor $S(q)$ for sodium silicate models with $x = 0.0$ and 0.3, respectively. The left and right subplots correspond to $T(r)$ and $S(q)$, respectively.

[35] with $x = 0.3$ is also displayed in the same plot for comparison. The BB model shows slightly better agreement of the second peak with the diffraction experiment than the model using the ReaxFF potential. The direct melt-quench model captures the second peak of $S(q)$ better than the BB model; nevertheless, overall agreement with the experiment is more or less similar. The large model using the ReaxFF potential captures the FSDP of the neutron diffraction experiment. The small-sized models with 240 atoms provide poor description of correlations in intermediate or extended length scales. The origin of the FSDPs in silica and alkali silicates are attributed to many factors such as system size, composition, etc., and are discussed in Refs. [15,36,37].

The left plot in Fig. 3 depicts $g(r)$ calculated from the models. For the model with $x = 0.0$, the first peak in $g(r)$ is located at ≈ 1.63 Å and corresponds to the Si-O correlations. $g(r)$ for the model with $x = 0.1$ shows that the first peak is slightly shifted towards the right at ≈ 1.64 Å. For the model with $x = 0.3$, $g(r)$ shows that the first major peak is further shifted to ≈ 1.65 Å. The calculated bond length for this model is closer to the Si-O bond length obtained from EXAFS measurement (1.66 ± 0.02 Å) than from neutron scattering measurements (1.62 Å) [4,33]. For the silica structure, Si tetrahedra are connected by bridging oxygen (BO) atoms. Addition of a modifier to such a structure depolymerizes the silica network by breaking the Si-BO-Si bonds and forming nonbridging oxygen (NBO) atoms. The concentrations of such NBO atoms in the doped models were calculated to be 7.24% (10.53) and 34.56% (35.29) with $x = 0.1$ and 0.3, respectively, where numbers inside the parentheses correspond to theoretical percentages assuming that each Na_2O creates two NBO atoms. The low percentage of NBO atoms for the model with $x = 0.1$ suggests that not all Na atoms depolymerize the network to form NBO atoms. The direct melt-quench model also contains the same number of NBO atoms as the BB model with $x = 0.3$, showing very similar structural topologies between

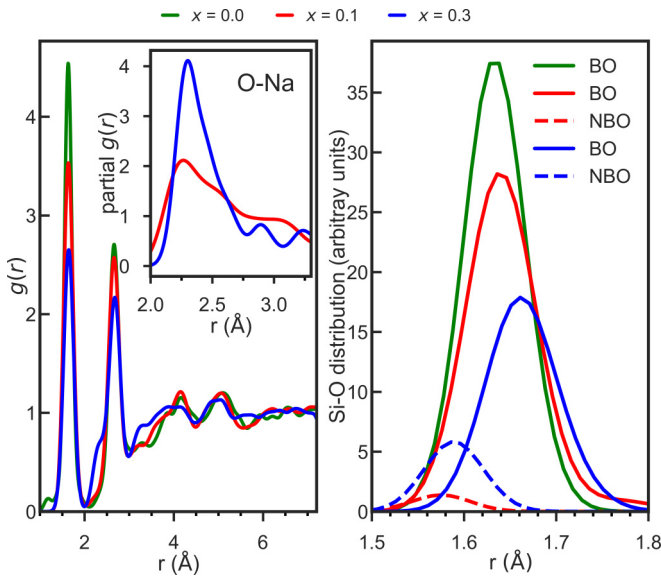


FIG. 3. Radial distribution function $g(r)$ (left) and bond length distribution of Si and O atoms (right) for $(\text{Na}_2\text{O})_x(\text{SiO}_2)_{1-x}$ models. The inset in the left plot shows partial $g(r)$ attributed to Na-O correlations for the doped models. Solid and dashed lines in legends in the right plot correspond to bonding of Si with bridging oxygen (BO) and nonbridging oxygen (NBO) atoms, respectively. NBO atoms here refer to O atoms that are linked to only one Si atom. BO atoms refer to O atoms that are not NBO atoms.

the models obtained from these two different methods. Earlier studies also obtained a similar percentage of NBO atoms for the model with $x = 0.3$ [14,38]. The fraction of BO and NBO atoms in the model with $x = 0.3$ is in agreement with results obtained using electron spectroscopy for chemical analysis [39]. From the left plot in Fig. 3, the intensity of the first peak in $g(r)$ is seen to decrease with increasing x . This is attributed to the formation of fewer Si-BO bonds with increase in x and can be explained from the bond distribution of Si with O atoms. The bond distribution for the $(\text{Na}_2\text{O})_x(\text{SiO}_2)_{1-x}$ models was calculated and the contributions from Si-BO and Si-NBO bonds are displayed in the right-hand plot of Fig. 3. It can be seen that the intensity of the Si-BO distribution decreases with increase in x that results in decreasing intensity of the first peak in $g(r)$. The shift in peak position of the Si-BO distribution towards larger distance results in an overall shift of the first peak in $g(r)$ with increasing x as observed in left plot of Fig. 3. The study by Sakka and Matusita [40] confirmed that the addition of Na_2O weakens the Si-O bond and results in an increase in Si-O bond length. This is consistent with our results and with the previous studies [33,41]. The Si-NBO bonds peak at lower bond length, ≈ 1.59 Å, and the peak intensity grows with increase in x . So, for a high concentration of Na_2O content in the silicates ($x \geq 0.5$), the first peak in $g(r)$ is expected to shift closer to the Si-NBO peak. For all models, the second peak at ≈ 2.66 Å is mainly due to O-O partial correlations. The calculated Si-Si correlations show a peak at ≈ 3.06 Å for the doped models. The Si-Si bond length for the models is very close to that obtained from the neutron diffraction experiments for α - SiO_2 (3.08 Å). Most of the DFT and classical MD studies predict

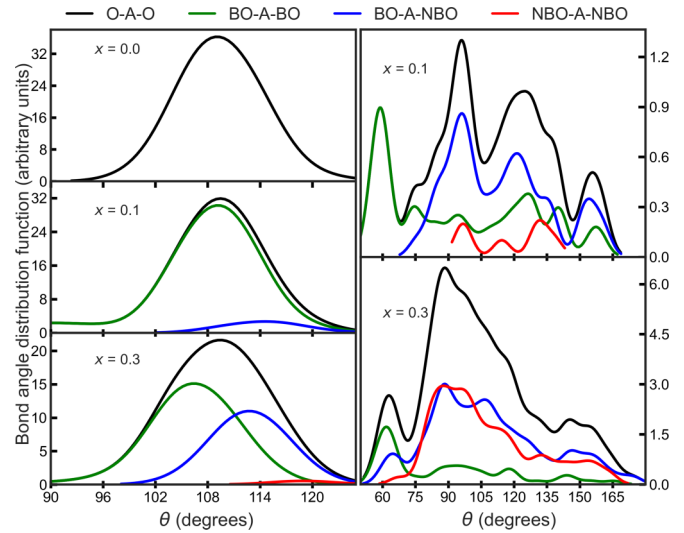


FIG. 4. Bond angle distribution functions for the $(\text{Na}_2\text{O})_x(\text{SiO}_2)_{1-x}$ models within the first cutoff distance for each atomic pair showing the contribution of BO and NBO atoms. “A” in the legend refers to either Si or Na atoms and the black solid line corresponds to the total distribution for each case. Left and right plots correspond to O-Si-O and O-Na-O angles, respectively. BO and NBO atoms used here are same as defined in Fig. 3.

the bond length of ≈ 3.11 – 3.19 Å for these glasses [42,43]. For both doped models, there exists a small minor peak at ≈ 2.3 Å which is due to the partial pair correlations from Na and O atoms forming a weak ionic bond. The inset in the left-hand plot of Fig. 3 shows that the intensity of this peak is large for the model with $x = 0.3$. This peak is mainly attributed to Na-NBO correlations in the network. The Na-BO correlations are found towards larger distance and form a peak at ≈ 2.42 Å.

The bond angle distribution function (BADF) for the models was also analyzed. Figure 4 displays BADFs corresponding to O-Si-O and O-Na-O angles. The left plot in Fig. 4 shows the BADF corresponding to O-Si-O angles. The BADF shows that O-Si-O angles for the models are approximately normally distributed. For the undoped model, O-Si-O bond angles form a peak at $\approx 108.9^\circ$ and have a full width at half maximum (FWHM) of 12.5° . The neutron diffraction experiment by Grimley *et al.* [32] found the peak at 109.7° with FWHM of 10.6° . The models obtained using potentials developed by Vessal *et al.* (VSL) [44] and by Beest *et al.* (BKS) [45] potentials show that the O-Si-O angles form a peak at 109.3° with a FWHM of 12.2° and at 108.6° with a FWHM of 15.1° , respectively [42]. For the doped models, it can be seen that the intensity of the BO-Si-BO distribution decreases with increase in x and is attributed to the formation of more NBO atoms in the network. The BO-Si-NBO angles are mostly formed towards the right of the tetrahedral angle and these angles form a broader peak at $\approx 112.0^\circ$ for the model with $x = 0.3$. On the other hand, BO-Si-O angles lie towards the left side and form a peak at $\approx 106.0^\circ$. There exists a negligible contribution from NBO-Si-NBO angles to the distribution at $\approx 119.0^\circ$ for the model with $x = 0.3$. The presence of more NBO atoms in the network causes an overall shift of the O-Si-O angles’ peak towards the high angle

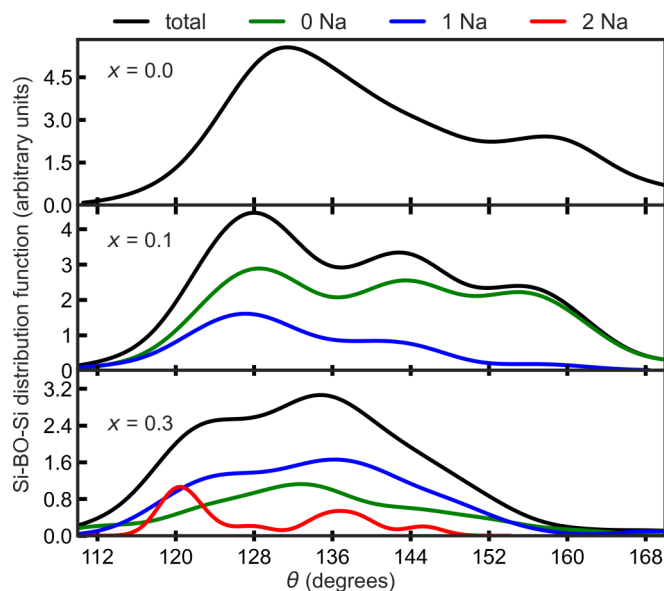


FIG. 5. Bond angle distribution functions corresponding to Si-BO-Si angles for the $(\text{Na}_2\text{O})_x(\text{SiO}_2)_{1-x}$ models shown by black lines in all plots. The distribution decomposed based on the number of modifier atoms (Na) that are linked to BO atoms is shown by the colored lines and labeled at the top of the figure for the doped models. The cutoff distance of 2.74 Å for Na-O pairs is used.

side. The BADF shows a peak at $\approx 109.5^\circ$ with a FWHM of 12.0° and at $\approx 109.7^\circ$ with a FWHM of 15.0° for the models with $x = 0.1$ and 0.3 , respectively. The study based on neutron diffraction experiment by Misawa *et al.* showed the O-Si-O angles for $x = 0.0$ and 0.33 to be 109.1° and 109.3° , respectively [41]. The classical MD simulations of the silicate glasses show peaks at slightly lower values for O-Si-O angles for the studied compositions [14,38,46,47].

The right-hand plot in Fig. 4 depicts the BADF corresponding to O-Na-O angles for the doped models. The BADF for the model with $x = 0.1$ shows that there exists a first peak at $\approx 59.0^\circ$ and corresponds to BO-Na-BO angles. For the model with $x = 0.3$, the first peak in the BADF lies at $\approx 62.9^\circ$ and is attributed to the BO-Na-BO, BO-Na-NBO, and NBO-Na-NBO angles with the smallest contribution from NBO-Na-NBO angles. Beyond the first peak, there exists another broad peak at $\approx 88.5^\circ$ and near the far end forming a shoulder at $\approx 150.0^\circ$. The major broad angle formed at $\approx 88.5^\circ$ is attributed to almost equal contributions from NBO-Na-NBO and BO-Na-NBO angles. The shoulder formed at the far side is also attributed to these angles. Such a broad peak does not exist for the model with $x = 0.1$ because of few available NBO atoms. There exist peaks at $\approx 95.9^\circ$ and 121.8° that are mostly attributed to BO-Na-NBO angles.

To understand how the tetrahedra are connected in the network, the BADFs corresponding to Si-BO-Si angles were calculated and are displayed in Fig. 5. Unlike the symmetric distribution obtained from most classical MD simulations [42,48], our simulations show that the bond angles are more spread out with the asymmetric shape of the distribution and are mostly biased towards small angles. Donadio *et al.* [49] have also shown that for the model with $x = 0.25$, *ab initio* Car-Parrinello MD results in a spread-out distribution

compared to the symmetric distribution from classical MD. The total BADF distribution for the undoped model shows a broad peak at $\approx 131.4^\circ$. The peak lies towards the small angle compared to the NMR secant model (142°) [50] and the x-ray diffraction model by Mozzi and Warren (144°) [51]. The latter model reproduces the asymmetric distribution of Si-BO-Si angles. For the undoped and slightly doped ($x = 0.1$) models, bond angles near the extremes are observed at $\approx 158^\circ$ and 160° , respectively. On the other hand, the distribution flattens in this region for the model with $x = 0.3$. Therefore, the distribution narrows and also shifts towards smaller angles with increasing x . This could be attributed to the increased Si-O lengths with addition of the modifier atoms [52]. The BADFs corresponding to the doped models were decomposed based on linking of the BO atoms with neighboring Na atoms and are displayed by colored lines in Fig. 5. It is observed that peaks at extremes are mostly attributed to the Si-BO-Si angles that are not linked to the modifier atoms. The Si-BO-Si angles with Na atoms as neighbors mostly form peaks towards small angles. For the model with $x = 0.3$, the Si-BO-Si angles linked with two Na atoms show a contribution to the peak very close to 120° but are absent for the model with $x = 0.1$. For the model with $x = 0.1$, there exist distinct peaks at $\approx 127.8^\circ$ and 142.8° . For the model with $x = 0.3$, there is a major peak at $\approx 134.8^\circ$ and a shoulder towards the small-angle side at $\approx 125.1^\circ$. It is observed that the contribution from the Si-BO-Si angles linked with one Na atom becomes higher with increase in x . A detailed analysis of Si-O-Si bond angle distribution for silica and sodium silicates can be found in Ref. [48].

To further understand the extent of depolymerization of the silica network due to the presence of the Na_2O modifier, the Q^n distribution of Si atoms was calculated. Q^n is defined as Si atoms with n BO atoms. The NBO atoms are defined as O atoms that only form a bond with one Si atom. The BO atoms here refer to O atoms that are not NBO atoms. For the model with $x = 0.0$, all O atoms form BO atoms and constitute 100% of the Q^4 distribution. The Q^n distribution for the doped models is displayed as histograms in Fig. 6. The Q^n distribution obtained from the doped model with $x = 0.3$ shows agreement with estimated values obtained from the NMR experiment shown by light blue histograms [53]. For the model with $x = 0.1$, it is observed that the structure has a majority of Q^4 (79.17%) and Q^3 (15.28%) distributions, which are displayed as red colored histograms in Fig. 6. A few Q^5 distributions are observed in both doped models and a Q^6 is observed for the model with $x = 0.1$. The contributions from Q^5 and Q^6 are very small, and could be artifacts of the high cooling rate used to quench the liquid phase to obtain the glass models. These are also sensitive to the cutoff used to define bond length between Si and O atoms. For the model with $x = 0.3$, the majority are Q^3 (66.07%) and Q^4 (23.21%). Simulated silicate glasses using classical MD or combined with DFT show similar results for the model with $x = 0.1$ whereas a significant deviation of Q^3 values is observed for the model with $x = 0.3$ [14,16,54].

In order to understand the local bonding environments of these glasses, the average coordination numbers for different atomic pairs were calculated. To describe the coordination, the covalent radius for each atom was used. So, the distance between atoms which is no more than the sum of covalent

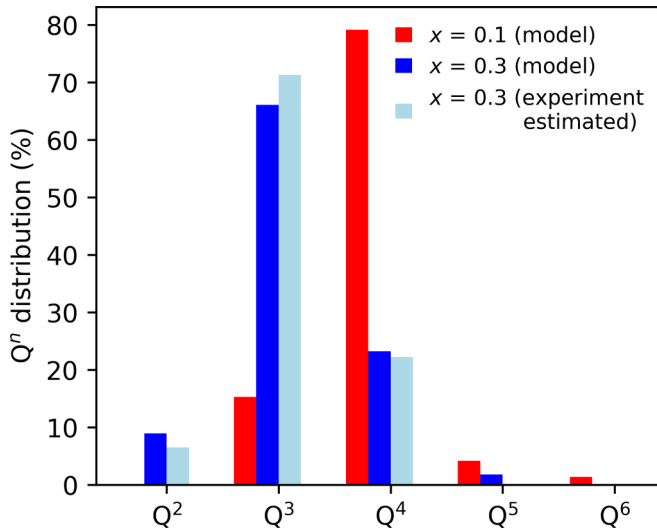


FIG. 6. Q^n distribution for the doped models. The red and blue bars correspond to the calculated Q^n from the relaxed models with $x = 0.1$ and 0.3 , respectively. The light blue bars correspond to the experimental data estimated for $x = 0.3$ from Ref. [53]. A cutoff distance of 1.94 \AA is used to define the bonds between Si and O atoms based on their covalent radii plus a tolerance factor of 0.10 \AA .

radii of the atomic pairs within the tolerance of 0.1 \AA only contribute to the coordination. The detailed coordination numbers for the doped glasses are shown in Table I.

Table I shows that the average coordination of each atom type is x dependent. It is clear that the mean coordination of each atom increases with increase in x . For the doped models, we find a significant increase in the average coordination of Na with increase in the Na_2O content. The coordination number was calculated to be 2.5 and 4.98 for models with $x = 0.1$ and 0.3 , respectively.

B. Electronic properties

For the doped models, as discussed in Sec. III A, the Na atoms modify the structural topology of the glass essentially by breaking the Si-BO-Si and forming NBO atoms; the effect escalates with increase in Na_2O content. This in turn induces a

TABLE I. Average coordination number (n) and its distribution among each atomic pair, $n()$, where () is filled by the corresponding atomic species. The coordination is counted only if the distance for each atomic pair is no more than the sum of their covalent radii plus a tolerance factor of 0.1 \AA . Covalent radii of 1.11 , 0.73 , and 1.66 \AA was taken for Si, O, and Na atoms, respectively.

Na_2O content (x)	Atom	n	$n(\text{Si})$	$n(\text{O})$	$n(\text{Na})$
0.0	Si	3.93	0.00	3.93	
	O	1.96	1.96	0.00	
0.1	Si	4.07	0.00	4.07	0.00
	O	2.17	1.93	0.00	0.24
	Na	2.5	0.0	2.25	0.25
0.3	Si	4.11	0.00	4.02	0.09
	O	2.73	1.65	0.00	1.07
	Na	4.98	0.10	3.04	1.83

variation of the electronic structure of the glass. To understand this, quantities like the electronic density of states (EDOS) were computed, and the localization of the states was gauged by the inverse participation ratio (IPR), defined as

$$\mathcal{I}(\psi_n) = \frac{\sum_1^N a_{ni}^4}{(\sum a_{ni}^2)^2}, \quad (3)$$

where a_{ni} are the contributions to the eigenfunction ψ_n from the i th projected atomic orbital obtained from VASP. In physical terms, it is the probability of finding a state ψ_n over the basis $\{a_{ni}\}_{i=1}^N$. The value of \mathcal{I} ranges from zero to 1. Larger \mathcal{I} signifies that the states are localized on fewer atomic sites, whereas the smaller \mathcal{I} indicates states are evenly distributed over many atomic sites.

The subplots in Fig. 7(a) show the total EDOS and the EDOS projected on atomic sites for the doped models. Electronic Kohn-Sham band gaps of ≈ 3.96 and ≈ 3.82 eV were observed for models with $x = 0.1$ and 0.3 , respectively. Quite large band gaps for glasses with the same composition have been reported by Murray and Ching [55] and are 5.82 and 4.61 eV for models with $x = 0.1$ and 0.3 , respectively. For the doped models, the top of the valence edge derives from NBO atoms and the bottom of the conduction band is from more or less all three species. The EDOS projected on atomic sites shows that the contribution of the Na ions in the conduction band increases with x , which is apparent from the inset plots in Fig. 7(a). The IPR values [labeled on right y axis in Fig. 7(a)] show that states near the valence edge are highly localized and are attributed to the nonbridging O $2p$ orbitals. The energy range of localization is slightly deeper into the valence band for the model with $x = 0.3$ than with $x = 0.1$, which is possibly due to comparatively more NBO atoms. For both doped models, defect states appear in the gap around 1 eV below the conduction edge and are shown by arrowheads in the inset plot in Fig. 7(a). The charge densities corresponding to these defects were then determined and are displayed as isosurface plots (purple blobs) in Figs. 7(b) and 7(d) for models with $x = 0.1$ and 0.3 , respectively. The isosurface plots show that the charge is mostly spatially localized in a few atomic sites for both models. For the model with $x = 0.1$, the maximum charge density is attributed to the Na atom towards the O-deficient center as shown in Fig. 7(c). The charge density is extended towards larger angles ($\approx 113^\circ$) of the SiO_4 tetrahedral unit. These sites serve as intrinsic charge carrier sites in the network. For the model with $x = 0.3$, the charge density is bounded by Na atoms towards the O-deficient sides of the network. Figure 7(e) shows the particular region within the supercell where the charge density is localized in space surrounded by four Na atoms. Increase in Na_2O content in the glass could lead to more such defect states near the conduction tail and could be engineered for optical applications.

C. Thermal properties

In this section, the thermal properties of the doped models are studied by calculating the linear thermal expansion coefficients (LTECs) and specific heat capacities at constant pressure (C_p). These properties are calculated using the quasi-harmonic approximation approach discussed in Sec. II B.

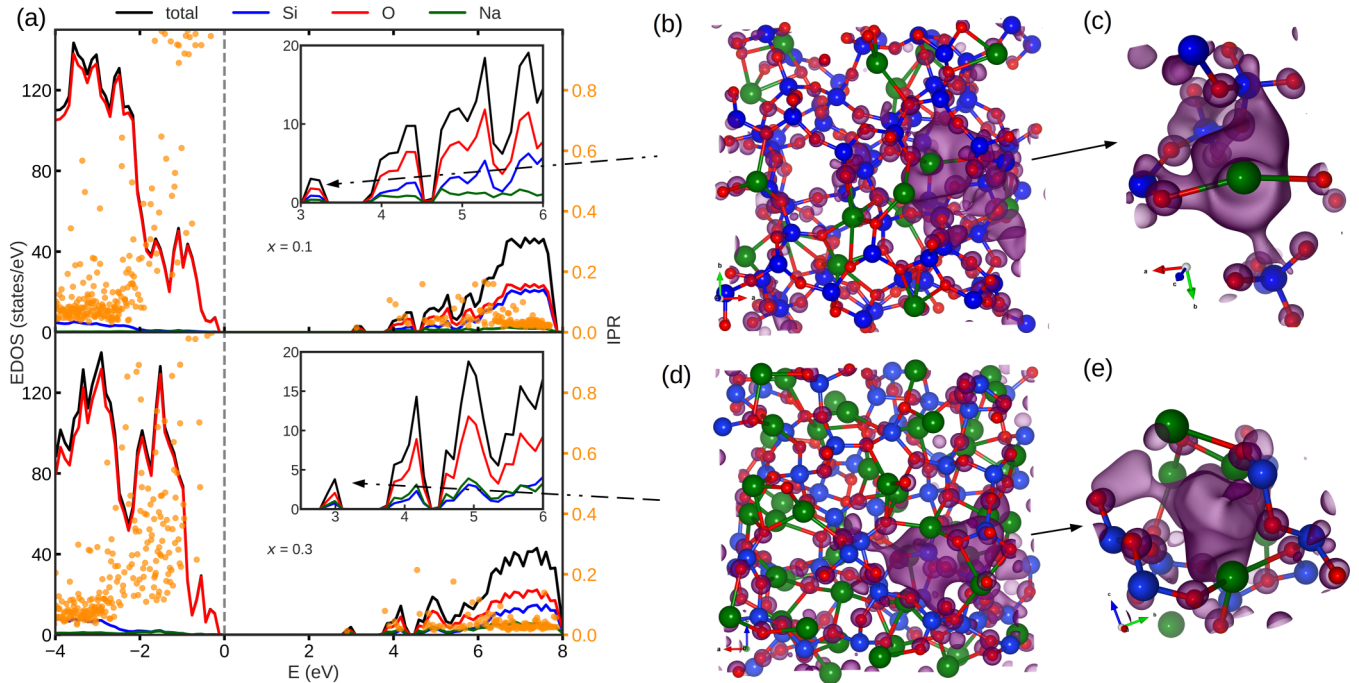


FIG. 7. (a) Total and projected electronic density of states, and the inverse participation ratio for $(\text{Na}_2\text{O})_x(\text{SiO}_2)_{1-x}$ models. (b, d) Partial charge density for the defect state in the gap shown as isosurface (purple colored blobs) plots for the doped models with $x = 0.1$ and 0.3 , respectively. (c, e) Close look of the defect sites in (b) and (d), respectively. Atom colors match with the legends in (a).

The temperature-dependent Helmholtz free energy $F(T, V)$ was obtained as discussed in Sec. II B, and is plotted for one of the doped models with $x = 0.3$ shown by solid circles in Fig. 8(a). The dashed lines represent the fit using the Birch-Murnaghan equation. The minimum volume from each curve was determined [indicated by the star symbol in Fig. 8(a)] and these volumes are plotted against the temperature in Fig. 8(b). The volume thermal expansion coefficient was obtained using the relation

$$\beta(T) = \frac{1}{V(T)} \frac{\partial(V(T))}{\partial T}. \quad (4)$$

The LTEC, denoted by α , was calculated assuming $\alpha = \frac{1}{3}\beta$ and compared with the experiment [56] that is measured at low temperatures. Figure 8(c) shows the calculated and the experimental values of α for both doped models. The calculated values of α for the model with $x = 0.3$ are in excellent agreement with the experimental values. The calculated value of α was determined to be $9.0 \times 10^{-6} \text{ K}^{-1}$, close to the experimental value $1.2 \times 10^{-5} \text{ K}^{-1}$ at 283 K. For $x = 0.1$, the LTEC values are about an order smaller than the experimental values at very low temperature but are closer to the experiment from around 80 K to room temperature. The calculated value of α was found to be $6.9 \times 10^{-6} \text{ K}^{-1}$ compared with the experimental value $5.0 \times 10^{-6} \text{ K}^{-1}$ at 283 K.

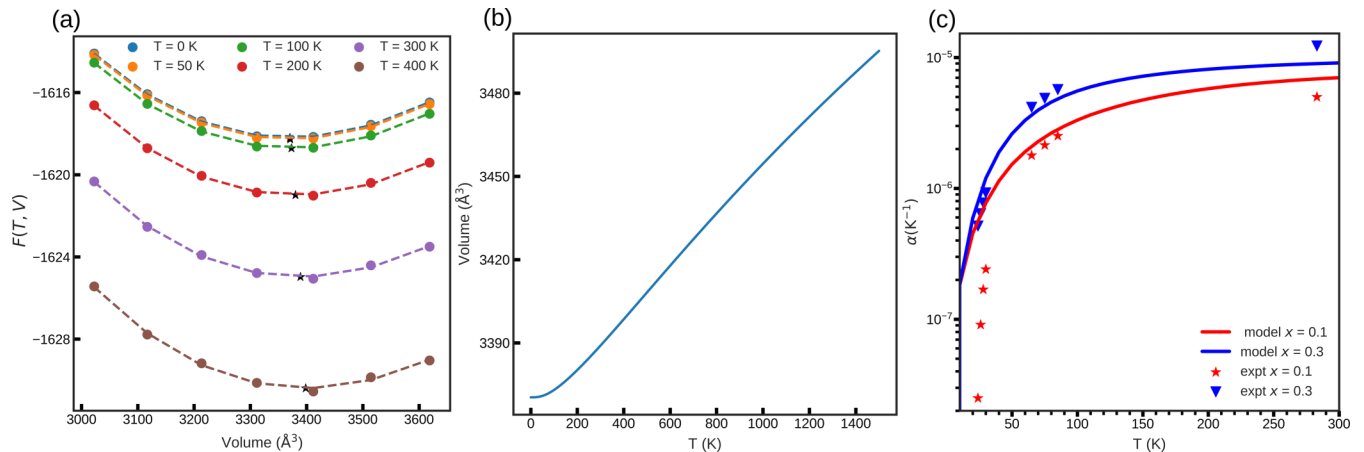


FIG. 8. (a) Helmholtz free energy obtained for seven different volumes at selected temperatures shown by the solid circles. The dashed lines represent the fit to the EOS. The black star symbols represent the Gibbs free energy. (b) The volume vs temperature plot for the doped model with $x = 0.3$. (c) Linear thermal expansion coefficient for both doped models.

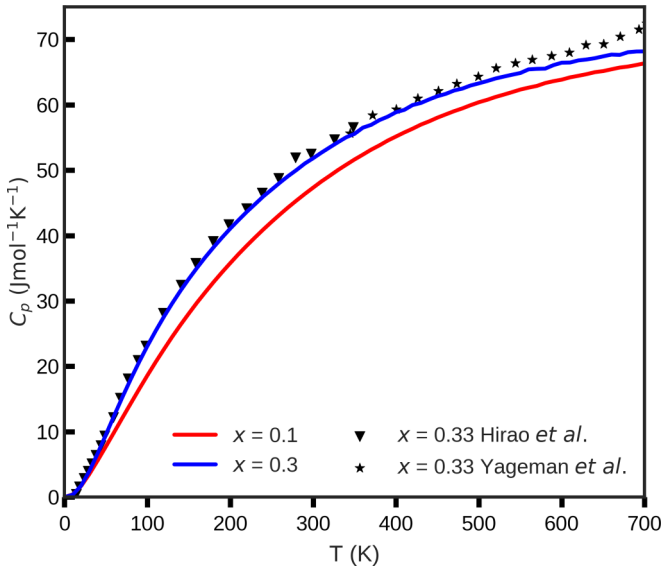


FIG. 9. Specific heat capacity at constant pressure (C_p) for $(\text{Na}_2\text{O})_x(\text{SiO}_2)_{1-x}$ models with $x = 0.1$ and 0.3 shown by solid lines and the experimental values for $x = 0.33$. The triangle and star symbols correspond to the values taken from Refs. [58,59].

From $F(T, V)$, the Gibbs free energy $G(T, p)$ at given temperature and pressure was obtained through the transformation

$$G(T, p) = \min_V [F(T, V) + pV]. \quad (5)$$

From $G(T, p)$, the thermal properties such as specific heat at constant pressure (C_p) can be calculated. Figure 9 shows the specific heat capacity at zero pressure for both doped models. The C_p for the model with $x = 0.3$ is slightly higher compared to $x = 0.1$ throughout the provided temperature range. The results for the model with $x = 0.3$ were compared with the closest available experimental results with $x = 0.33$ and are shown by scattered plots in Fig. 9. It can be seen that the results are in close agreement. The heat capacity for the sodium silicate glasses obtained from classical MD also shows a similar result [57]. For these doped models, the calculated values of C_p at 300 K were obtained to be 51.86 and 47.38 $\text{J mol}^{-1} \text{K}^{-1}$ with $x = 0.3$ and 0.1 , respectively. The experimental value for $x = 0.33$ at this temperature is 52.50 $\text{J mol}^{-1} \text{K}^{-1}$.

D. Elastic properties

The elastic properties for the models are studied from the elastic tensor (C_{ij}). C_{ij} can be obtained by distorting the lattice vectors and relaxing all of the internal parameters to minimize the total energy. The distortion of the lattice vectors results in a change in total energy by an amount [60]

$$E(e_i) = E_0 - P(\Omega)\Delta\Omega + \Omega \sum_{i=1}^6 \sum_{j=1}^6 C_{ij} e_i e_j / 2 + O[e_i^3], \quad (6)$$

where Ω is the volume of the undistorted lattice, $P(\Omega)$ is the pressure of the undistorted lattice at the volume Ω , $\Delta\Omega$ is the change in the volume of the lattice due to the acting strain,

TABLE II. Elastic properties obtained from $(\text{Na}_2\text{O})_x(\text{SiO}_2)_{1-x}$ models.

Na ₂ O content	Bulk modulus (GPa)			Shear modulus (GPa)		
	K_V, K_R, K_{avg}			G_V, G_R, G_{avg}		
0.0 Model	34.02, 32.25, 33.18			25.28, 22.81, 24.05		
Expt.	36.10			31.25		
0.1 Model	27.92, 23.48, 25.70			25.53, 22.28, 23.91		
Expt.	33.95			27.68		
0.3 Model	34.56, 33.75, 34.16			22.62, 21.37, 21.99		
Expt.	39.03			23.80		

and the third-order term of e_i has been neglected. Altogether, there are 21 independent C_{ij} in Eq. (6). However, symmetry reduces the number of independent C_{ij} depending upon the crystal structure. By the means of the C_{ij} and the compliance tensor, s_{ij} (C_{ij}^{-1}), the bulk modulus (K) and shear modulus (G) can be expressed as [61]

$$9K_V = (C_{11} + C_{22} + C_{33}) + 2(C_{12} + C_{23} + C_{31}), \quad (7)$$

$$15G_V = (C_{11} + C_{22} + C_{33}) - (C_{12} + C_{23} + C_{31}) + 3(C_{44} + C_{55} + C_{66}), \quad (8)$$

$$1/K_R = (s_{11} + s_{22} + s_{33}) + 2(s_{12} + s_{23} + s_{31}), \quad (9)$$

$$15/G_R = 4(s_{11} + s_{22} + s_{33}) - 4(s_{12} + s_{23} + s_{31}) + 3(s_{44} + s_{55} + s_{66}), \quad (10)$$

where C_{ij} are written according to Voigt notation [62]. The expressions for K and G with subscripts V and R in Eqs. (7)–(10) refer to the Voigt and Reuss approaches of determining the bulk and shear modulus, respectively. The Voigt approach provides an upper limit and the Reuss approach provides the lower limit.

The stress tensor C_{ij} for each doped model was obtained from VASP using a strain of 0.015 Å. The diagonalization of the matrix C_{ij} was then performed that yielded positive eigenvalues satisfying the elastic stability. The calculated bulk and shear moduli are presented in Table II and are compared with experiment [63].

From Table II, it can be seen that the calculated values of shear and bulk moduli using the Voigt approach are closer to the experimental data for all the models. But for better comparison with the experiment, the average of the values from both Voigt and Reuss approaches was performed. These quantities are denoted as K_{avg} and G_{avg} for bulk and shear modulus, respectively, in Table II. We see that the calculated values of G_{avg} for both doped models are close to the experimental values with maximum deviation of 3.77 GPa. For the undoped model, we find the deviation of 7.20 GPa from the experiment. The calculated K_{avg} for the undoped and $x = 0.3$ models are also closer to the experimental value (deviation < 5 GPa). For the model with $x = 0.1$, the calculated K_{avg} was found to be quite low compared with the experimental value (deviation of 8.25 GPa). The discrepancies of similar range and even higher than the tabulated values have been reported in the literature [15,64–66].

IV. CONCLUSIONS

The realistic models of $(\text{Na}_2\text{O})_x(\text{SiO}_2)_{1-x}$ glasses were obtained using the building-block method that is potentially suited for predicting the structure of the homogeneous glasses. Structural properties of the models were explored by studying the correlation functions such as pair-correlation functions, structure factors, bond angle distribution functions, Q^n distributions, and the local coordination analysis. The pair-correlation functions calculated from the obtained models show that the BB method correctly predicts the local structure of the glasses and also captures the signature of the medium-range order. The Si-O bond length is found to be increased with increase in Na_2O content for the studied concentrations and is consistent with the previous studies. The bond angle distribution functions corresponding to Si-BO-Si angles are found to be narrower and O-Si-O angles shift slightly towards the higher angle with increase in modifier concentration. The Q^n distribution for the fully doped model shows good agreement with the NMR studies. The electronic density of states for the doped glasses shows the presence of defect states in the band gap towards the conduction tail and that are mostly

localized at undercoordinated Na atoms in the network. The thermal properties of the doped models were computed on the basis of quasiharmonic approximation. The calculated values of linear thermal expansion coefficient show satisfactory agreement with the experiment. The specific heat capacity for the doped models was calculated and the fully doped model shows that the results are in agreement with the experiment. The elastic properties of the doped models were also studied by calculating the bulk and shear moduli, and these values also satisfactorily agree with the experimental values.

ACKNOWLEDGMENTS

The authors acknowledge the National Science Foundation (NSF) for support under DMR award 1507670. The authors also acknowledge the Extreme Science and Engineering Discovery Environment (XSEDE), supported by NSF Grant No. ACI-1548562 at the Pittsburgh Supercomputer Centers for providing computational resources under allocation DMR-190008P. The authors thank Dr. Kiran Prasai for valuable discussions during this work.

-
- [1] M. Lopes, in *Introduction to Glass Science and Technology* (Royal Society of Chemistry, Cambridge, U.K., 2005), pp. X001–X004.
- [2] E. M. Vogel, *J. Am. Ceram. Soc.* **72**, 719 (1989).
- [3] A. Oliveira, P. Malafaya, and R. Reis, *Biomaterials* **24**, 2575 (2003).
- [4] G. Henderson, *J. Non-Cryst. Solids* **183**, 43 (1995).
- [5] R. Dupree, D. Holland, P. McMillan, and R. Pettifer, *J. Non-Cryst. Solids* **68**, 399 (1984).
- [6] J. Emerson, P. Stallworth, and P. Bray, *J. Non-Cryst. Solids* **113**, 253 (1989).
- [7] H. Nesbitt, G. Henderson, G. Bancroft, and R. Ho, *J. Non-Cryst. Solids* **409**, 139 (2015).
- [8] M. Fábíán, P. Jóvári, E. Sváb, G. Mészáros, T. Proffen, and E. Veress, *J. Phys.: Condens. Matter* **19**, 335209 (2007).
- [9] D. A. Drabold, *Eur. Phys. J. B* **68**, 1 (2009).
- [10] M. Bauchy, *J. Chem. Phys.* **137**, 044510 (2012).
- [11] X. Li, W. Song, K. Yang, N. M. A. Krishnan, B. Wang, M. M. Smedskjaer, J. C. Mauro, G. Sant, M. Balonis, and M. Bauchy, *J. Chem. Phys.* **147**, 074501 (2017).
- [12] A. Pandey, P. Biswas, and D. A. Drabold, *Phys. Rev. B* **92**, 155205 (2015).
- [13] Q. Zhou, T. Du, L. Guo, M. M. Smedskjaer, and M. Bauchy, *J. Non-Cryst. Solids* **536**, 120006 (2020).
- [14] J. Du and A. Cormack, *J. Non-Cryst. Solids* **349**, 66 (2004).
- [15] J. Du and L. R. Corrales, *J. Non-Cryst. Solids* **352**, 3255 (2006).
- [16] M. Pota, A. Pedone, G. Malavasi, C. Durante, M. Cocchi, and M. Menziani, *Comput. Mater. Sci.* **47**, 739 (2010).
- [17] L. Deng, S. Urata, Y. Takimoto, T. Miyajima, S. H. Hahn, A. C. T. van Duin, and J. Du, *J. Am. Ceram. Soc.* **103**, 1600 (2020).
- [18] K. Baral and W.-Y. Ching, *J. Appl. Phys.* **121**, 245103 (2017).
- [19] H. Jabraoui, Y. Vaills, A. Hasnaoui, M. Badawi, and S. Ouaskit, *J. Phys. Chem. B* **120**, 13193 (2016).
- [20] P. K. Hung, F. Noritake, L. T. San, T. B. Van, and L. T. Vinh, *Eur. Phys. J. B* **90**, 1 (2017).
- [21] B. Cai, X. Zhang, and D. A. Drabold, *Phys. Rev. B* **83**, 092202 (2011).
- [22] L. Ouyang and W. Y. Ching, *Phys. Rev. B* **54**, R15594 (1996).
- [23] G. Kresse and J. Furthmuller, *Phys. Rev. B* **54**, 11169 (1996).
- [24] O. Mazurin and Y. Gankin, *J. Non-Cryst. Solids* **342**, 166 (2004).
- [25] J. P. Perdew, K. Burke, and M. Ernzerhof, *Phys. Rev. Lett.* **77**, 3865 (1996).
- [26] S. Nosé, *J. Chem. Phys.* **81**, 511 (1984).
- [27] N. Shuichi, *Prog. Theor. Phys. Suppl.* **103**, 1 (1991).
- [28] D. M. Bylander and L. Kleinman, *Phys. Rev. B* **46**, 13756 (1992).
- [29] F. Birch, *Phys. Rev.* **71**, 809 (1947).
- [30] F. D. Murnaghan, *Proc. Natl. Acad. Sci. USA* **30**, 244 (1944).
- [31] A. Togo and I. Tanaka, *Scr. Mater.* **108**, 1 (2015).
- [32] D. I. Grimley, A. C. Wright, and R. N. Sinclair, *J. Non-Cryst. Solids* **119**, 49 (1990).
- [33] A. C. Wright, A. G. Clare, B. Bachra, R. N. Sinclair, A. C. Hannon, and B. Vessal, *Trans. Am. Crystallogr. Assoc.* **27**, 239 (1991).
- [34] P. A. Johnson, A. C. Wright, and R. N. Sinclair, *J. Non-Cryst. Solids* **58**, 109 (1983).
- [35] Y. Yu, B. Wang, M. Wang, G. Sant, and M. Bauchy, *Int. J. Appl. Glass Sci.* **8**, 276 (2017).
- [36] A. Nakano, R. K. Kalia, and P. Vashishta, *J. Non-Cryst. Solids* **171**, 157 (1994).
- [37] J. Du and L. R. Corrales, *Phys. Rev. B* **72**, 092201 (2005).
- [38] C. Huang and A. N. Cormack, *J. Chem. Phys.* **93**, 8180 (1990).
- [39] J. Jen and M. Kalinowski, *J. Non-Cryst. Solids* **38-39**, 21 (1980).
- [40] S. Sakka and K. Matusita, *J. Non-Cryst. Solids* **22**, 57 (1976).
- [41] M. Misawa, D. Price, and K. Suzuki, *J. Non-Cryst. Solids* **37**, 85 (1980).

- [42] X. Yuan and A. Cormack, *J. Non-Cryst. Solids* **283**, 69 (2001).
- [43] T. F. Soules, *J. Chem. Phys.* **71**, 4570 (1979).
- [44] B. Vessal, M. Amini, and C. Catlow, *J. Non-Cryst. Solids* **159**, 184 (1993).
- [45] B. W. H. van Beest, G. J. Kramer, and R. A. van Santen, *Phys. Rev. Lett.* **64**, 1955 (1990).
- [46] S. Ispas, M. Benoit, P. Jund, and R. Jullien, *Phys. Rev. B* **64**, 214206 (2001).
- [47] R. Murray, L. Song, and W. Ching, *J. Non-Cryst. Solids* **94**, 133 (1987).
- [48] X. Yuan and A. Cormack, *J. Non-Cryst. Solids* **319**, 31 (2003).
- [49] D. Donadio, M. Bernasconi, and F. Tassone, *Phys. Rev. B* **70**, 214205 (2004).
- [50] R. Pettifer, R. Dupree, I. Farnan, and U. Sternberg, *J. Non-Cryst. Solids* **106**, 408 (1988).
- [51] R. L. Mozzi and B. E. Warren, *J. Appl. Crystallogr.* **2**, 164 (1969).
- [52] G. V. Gibbs, M. M. Hamil, S. J. Louisnathan, L. S. Bartell, and H. Yow, *Am. Mineral.* **57**, 1578 (1972).
- [53] H. Maekawa, T. Maekawa, K. Kawamura, and T. Yokokawa, *J. Non-Cryst. Solids* **127**, 53 (1991).
- [54] N. Adelstein, C. S. Olson, and V. Lordi, *J. Non-Cryst. Solids* **430**, 9 (2015).
- [55] R. Murray and W. Ching, *J. Non-Cryst. Solids* **94**, 144 (1987).
- [56] G. White, J. Birch, and M. H. Manghnani, *J. Non-Cryst. Solids* **23**, 99 (1977).
- [57] N. Zotov, *J. Phys.: Condens. Matter* **14**, 11655 (2002).
- [58] K. Hirao, N. Soga, and M. Kunugp, *J. Am. Ceram. Soc.* **62**, 570 (1979).
- [59] V. D. Yageman and G. M. Matveev, *Fiz. Khim. Stekla* **8**, 238 (1982).
- [60] M. J. Mehl, B. M. Klein, and D. A. Papaconstantopoulos, in *Intermetallic Compounds: Principles*, edited by J. H. Westbrook and R. L. Fleischer (Wiley, New York, 1994), Vol. 1, p. 195.
- [61] R. Hill, *Proc. Phys. Soc. London Sect. A* **65**, 349 (1952).
- [62] W. Voigt, *Lehrbuch der kristallphysik* (Teubner, Leipzig, 1928).
- [63] N. P. Bansal and R. H. Doremus, *Handbook of Glass Properties* (Academic press, New York, 1986).
- [64] A. I. Priven, *Glass Technol.* **45**, 244 (2004).
- [65] A. Pedone, G. Malavasi, M. C. Menziani, A. N. Cormack, and U. Segre, *J. Phys. Chem. B* **110**, 11780 (2006).
- [66] A. Pedone, G. Malavasi, A. N. Cormack, U. Segre, and M. C. Menziani, *Chem. Mater.* **19**, 3144 (2007).